Rhombohedral Prussian White as Cathode for Rechargeable Sodium-Ion Batteries

15 AUTHORS, INCLUDING:

Jie Song
Massachusetts Institute of Technology
34 PUBLICATIONS   **418** CITATIONS

SEE PROFILE

L. Andrew Wray
Stanford University
96 PUBLICATIONS   **4,914** CITATIONS

SEE PROFILE

Yi-De Chuang
Lawrence Berkeley National Laboratory
101 PUBLICATIONS   **1,370** CITATIONS

SEE PROFILE

Rhombohedral Prussian White as Cathode for Rechargeable Sodium-Ion Batteries

Long Wang,[†,∇] Jie Song,[‡,∇] Ruimin Qiao,[§] L. Andrew Wray,[§,⊥,#] Muhammed A. Hossain,[§] Yi-De Chuang,[§] Wanli Yang,[§] Yuhao Lu,*[,†] David Evans,[†] Jong-Jan Lee,[†] Sean Vail,[†] Xin Zhao,[†] Motoaki Nishijima,[∥] Seizoh Kakimoto,[∥] and John B. Goodenough[‡]

[†]Sharp Laboratories of America, Camas, Washington 98607, United States

[‡]The University of Texas at Austin, Austin, Texas 78712, United States

[§]Advanced Light Source, Lawrence Berkeley National Laboratory, Berkeley, California 94720, United States

[∥]Corporate Research & Development Division (CRDD), Sharp Corporation, Tenri 632-8567, Japan

[⊥]Department of Physics, New York University, New York, New York 10003, United States

[#]Stanford Institute for Materials and Energy Sciences, SLAC National Accelerator Laboratory, 2575 Sand Hill Road, Menlo Park, California 94025, United States

S *Supporting Information*

ABSTRACT: A novel air-stable sodium iron hexacyanoferrate (R-$Na_{1.92}Fe[Fe(CN)_6]$) with rhombohedral structure is demonstrated to be a scalable, low-cost cathode material for sodium-ion batteries exhibiting high capacity, long cycle life, and good rate capability. The cycling mechanism of the iron redox is clarified and understood through synchrotron-based soft X-ray absorption spectroscopy, which also reveals the correlation between the physical properties and the cell performance of this novel material. More importantly, successful preparation of a dehydrated iron hexacyanoferrate with high sodium-ion concentration enables the fabrication of a discharged sodium-ion battery with a non-sodium metal anode, and the manufacturing feasibility of low cost sodium-ion batteries with existing lithium-ion battery infrastructures has been tested.
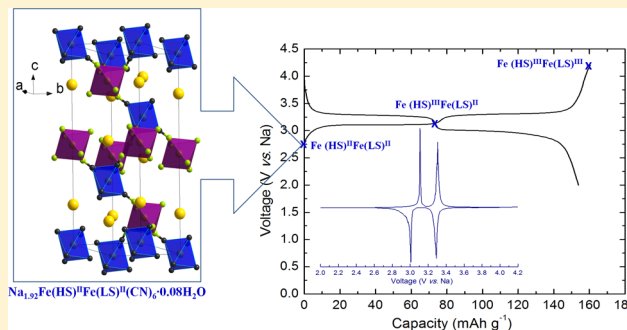
INTRODUCTION

The rapid growth of electrical energy from renewable but variable solar and wind power has created an urgent demand for an economic mean of storing this energy to enable its smooth integration into the grid and smart management of the grid-scale diurnal shift in peak energy demand. Rechargeable room-temperature batteries have several advantages for this application, including scale flexibility, economic maintenance, and energy-storage efficiency, compared to other energy-storage technologies such as fly wheels, pumped water, compressed air, and high-temperature sodium/sulfur batteries. However, meeting the cost target of less than $100/kWh for electrical energy storage with modification of Li-ion batteries powering hand-held electronic devices is proving to be a formidable challenge.

Sodium-ion batteries with insertion-compound cathodes analogous to the cathodes of lithium-ion batteries offer a higher energy density than aqueous batteries and lower cost than lithium-ion batteries.[1] The layered oxides and framework structures containing $(XO_4)^{n-}$ polyanions[2] that have been studied as cathodes for Na-ion batteries show a limited capacity that is further reduced in a cell that must be fabricated in a discharged state with an anode devoid of Na atoms. In addition, their high-temperature synthesis is a process of high energy consumption. On the other hand, Prussian-blue analogues (PBAs) with the general chemical formula $Na_{2-x}M_a[M_b(CN)_6]_{1-y} \cdot zH_2O$ are framework structures synthesized at low temperature that support a reversible extraction of two Na/formula unit (f.u.) at high rates with good cycle life.

The $(C \equiv N)^-$ anions of the double-perovskite $M_a[M_b(CN)_6]$ framework are ordered to create low-spin (LS) M_bC_6 and high-spin (HS) M_aN_6 octahedra. Considering their low cost and easy accessibility, hexacyanoferrates (M_b = Fe) are considered superior over other PBAs as electrode candidates. $Na_2NiFe(CN)_6$ and $Na_2CuFe(CN)_6$ have been studied for sodium ion insertion and extraction, but they only allow reversible extraction of one Na ion in a preferable voltage range showing a low capacity.[3,4] In our previous work,[5,6] sodium manganese hexacyanoferrate ($Na_{2-x}MnFe(CN)_6$) was identified to be a promising cathode of a Na-ion battery because the Mn(III)/(II) and Fe(III)/(II) redox couples were
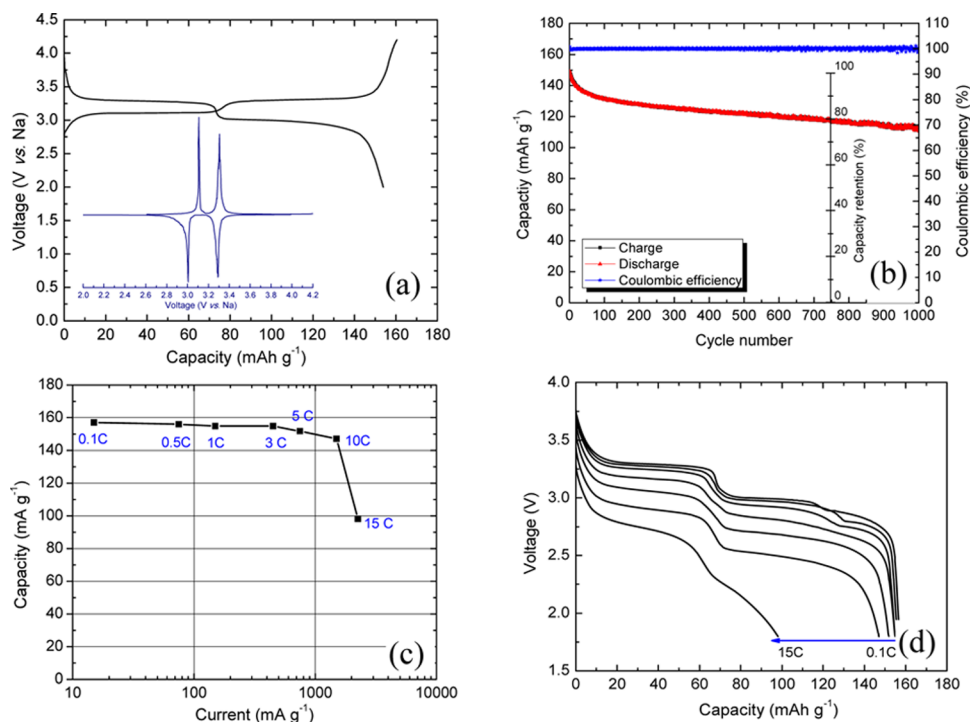
Figure 1. Electrochemical performance of a R-FeHCF electrode consisting of 86 wt % active material, 7 wt % Ketjen black, and 7 wt % PTFE. (a) Galvanostatic charge and discharge curves at a current of 10 mA g^{-1} at the first cycle (chronoamperograms were embedded). (b) Capacity retention of a R-FeHCF/Na half-cell in 1000 cycles (start from 1st cycle). It was charged at 0.5 C (75 mA g^{-1}) and discharged at 2C (300 mA g^{-1}). (c) Rate capability of the R-FeHCF/Na half-cell. It was charged at 0.1 C (15 mA g^{-1}) and discharged at different currents. (d) Discharge curves of the R-FeHCF/Na half-cell at different currents.

both accessible to give a large capacity within the favorable voltage range for Na batteries. The M$_a$[M$_b$(CN)$_6$] framework containing Fe as the only transition metal element (M$_a$ = M$_b$ = Fe) is very attractive for large-scale applications in terms of cost and resource abundance. Berlin green FeFe(CN)$_6$ has been reported to have a reversible capacity of 120 mAh g^{-1} with 87% capacity retention over 500 cycles.[7] However, a high Na concentration in the initial Na$_{2-x}$Fe[Fe(CN)$_6$] framework is desired to enable using a non-sodium metal anode to make practical Na-ion batteries. Very recently an acid-assisted method was used to synthesize Na$_y$Fe[Fe(CN)$_6$] with various sodium compositions ($y = 0.37-1.39$),[8] yet the as-shown low Coulombic efficiency and bizarre charge/discharge curves raise concerns of its application in full-cells.

In this paper, we report the synthesis of sodium iron hexacyanoferrate (sodium FeHCF or Na$_{2-x}$FeHCF) with a small x that demonstrates a superior performance as a cathode in a Na-ion battery. Compared with previous work, the high Na concentration in the new material overcomes the sodium-deficiency problem. We show that it could be directly assembled into a full cell with a hard carbon anode. This is critical for the scalable sodium-ion battery manufacture that is compatible with the current lithium-ion battery infrastructures. Furthermore, through synchrotron-based soft X-ray absorption spectroscopy (sXAS) and theoretical calculations, we clarify the cycling redox and fundamental mechanism of the electro-chemical cycling of the materials. The origins of the cycling plateaus are clearly explained based on the different Fe-3d states at different sites. The spectroscopic results also suggest the highly itinerant electron states, which is consistent with the high rate performance.

RESULTS AND DISCUSSION

Structural and Half-Cell Data. From powder XRD, elemental analysis, and thermogravimetric analysis (TGA), the as-synthesized Na$_{2-x}$FeHCF of the present study is taken to be rhombohedral Na$_{1.92}$Fe$_2$(CN)$_6$ (R-FeHCF) as shown in Figure S1a (Supporting Information). A negligible water content (0.08 H$_2$O/f.u.) is assumed on the basis of only a small weight loss in the interval 50 < T < 180 °C that can be ascribed to adsorbed water before sample decomposition, Figure S1b. In the absence of interstitial water, the Na$_{2-x}$FeHCF is rhombohedral $R\overline{3}$ with a cooperative rotation of the FeN$_6$ and FeC$_6$ octahedra that retains straight (C≡N)$^-$ anions and a displacement of the Na$^+$ along $a[111]$ axis toward a high-spin (HS) Fe^{II}N$_6$ octahedron, which is an isostructure of Na$_2$MnMn(CN)$_6$.[9] The D-STEM electron diffraction pattern also confirms its rhombohedral structure (Figure S1c). The morphology of the as-synthesized sample is shown in Figure S1d.

Figure 1a shows the voltage profiles on charge and discharge of R-FeHCF in a Na half-cell with a current of 10 mA g^{-1}; the two different voltages are for the Fe^{III}/Fe^{II} redox energies of the HS-FeN$_6$ and LS-FeC$_6$ octahedra over, respectively, 0.08 < x < 1 and 1 < x < 2. The high initial Na concentration is reflected in a capacity ~160 mAh g^{-1} in the first cycle, which corresponds to an energy density of ~490 Wh/kg. In comparison with an initially reported cubic FeHCF,[7] the R-FeHCF shows much flatter two-phase voltage profiles and sharper peaks in the chronoamperograms, as shown in the inset of Figure 1a, which indicates the first-order transitions between these structures during charge/discharge. The voltages of the two plateaus are at 3.11 and 3.30 V on charge, 3.00 and 3.29 V on discharge. Later in this work, sXAS results and theoretical simulation clarify that

the high and low voltage plateaus correspond to the oxidation/reduction of the LS-FeC$_6$ and HS-FeN$_6$ octahedra, respectively. As shown in Figure 1b, both redox reactions exhibit excellent reversibility with 80% of the initial capacity retained after 750 cycles of a Na half-cell. With negligible interstitial water, R-FeHCF demonstrates a high Coulombic efficiency from the first cycle.

The initial color of the as-synthesized sample is white (Prussian white = PW = R-FeHCF). After washing and centrifuging, the color changed to a pale blue as a result of Na loss from the surface to give a nominal Na$_{1.92}$FeHCF. The color with 1 Na/f.u. is blue (Prussian blue = PB), and the color with no sodium is green (Berlin green = BG). Those color changes reflect changes in the frequency of the stretching mode of the cyano anion. Ex situ XRD and Raman spectra taken at different states of charge in the charge/discharge cycle are shown in Figure S2. The structural data show a reversible $R\bar{3}$-cubic-$R\bar{3}$ structural evolution upon Na extraction and reinsertion. The cubic phase at the end of charge has its XRD peaks shifted to lower angles compared to those with 1 Na/f.u. The Raman data taken at the same states of charge as the XRD data show the evolution of the C≡N$^-$ stretching mode with the structural changes. Three peaks at 2070, 2110, and 2150 cm^{-1} are observed in the Raman spectrum of the as-synthesized PW sample. Only the first two peaks are attributed to rhombohedral PW phase and the one at 2150 cm^{-1} is ascribed to a PB phase on the PW surface resulting from the loss of 0.08 Na/f.u. during preparation. The PB surface phase contributes to the air stability of the as-synthesized compound. At the end of charge, nearly all Na are removed and the Raman spectrum of the BG phase exhibits two peaks at 2170 and 2200 cm^{-1} with the presence of the PB peak 2150 cm^{-1}. As observed in the ex situ XRD data, the PW $R\bar{3}$ phase is restored, as confirmed by the Raman spectra, on reinsertion of 2 Na, but with no 2150 cm^{-1} peak of the PB phase, which accounts for a small excess of the discharge versus charge capacity in the first cycle (FEC was not used in these cells).

Figure 1c,d show the rate capability of Na extraction and reinsertion upon R-FeHCF in a Na half-cell. The discharge capacity of the R-FeHCF electrode, which contains 86 wt % active material, 7 wt % Ketjen black, and 7 wt % polytetrafluoroethylene (PTFE) binder, dropped from 157 to 145 mAh g^{-1} on increasing the current from 0.1 C (15 mA g^{-1}) to 10 C (1500 mA/g). This high rate capability and capacity are much greater than those in previous reports[9,10] for cubic Na$_{2-x}$FeHCF ($x > 1$) electrodes. Interestingly, the discharge capacity drops abruptly at 15 C, Figure 1c, as a result of a greater capacity loss at the low-voltage plateau, Figure 1d, which signals a slower rate of reduction of HS-Fe^{III}N$_6$ octahedra than of the LS-Fe^{III}C$_6$ octahedra.

Redox and Cycling Mechanism. sXAS reveals the energy and character of the unoccupied electronic states in the vicinity of the Fermi energy E_F, which fingerprints the formal valence, chemical potential, and elemental and orbital character of an active redox center.[11] Two different probe depths can be achieved, 10 and 100 nm, through total-electron-yield (TEY) and total-fluorescence-yield (TFY) modes, respectively.[12] Here we performed sXAS of all the elements including Fe-L (Figures 2, 3 and S4), C/N-K (Figures 4 and S5), and Na-K (Figure S6) edges. In particular, the Fe-L sXAS edges provide a direct and sensitive measure to obtain the Fe-3d fraction of the hybridized 3d and ligand-2p empty wave functions near the E_F of an active redox center as a function of its valence and spin state.[13] The
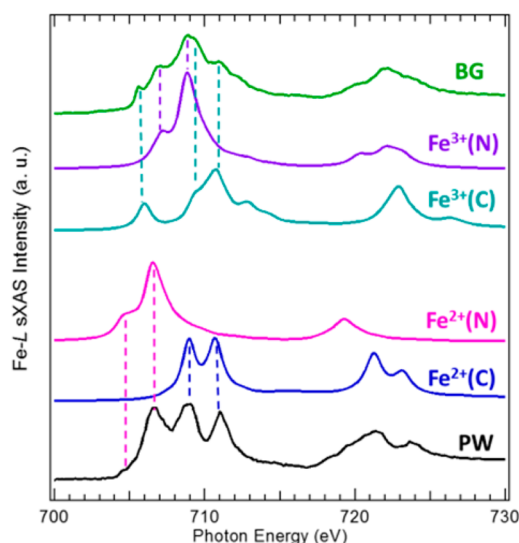

Figure 2. Experimental Fe L-edge sXAS spectra of Prussian White (PW) and Berlin Green (BG), compared with calculated spectra of Fe^{2+} and Fe^{3+} coordinated octahedrally with the C or N site of cyano groups. The resolved experimental features could be clearly assigned to Fe atoms at different sites with the specified formal valence. Herein, BG was synthesized from the FeCl$_3$ and K$_3$Fe(CN)$_6$ in solution.[7]
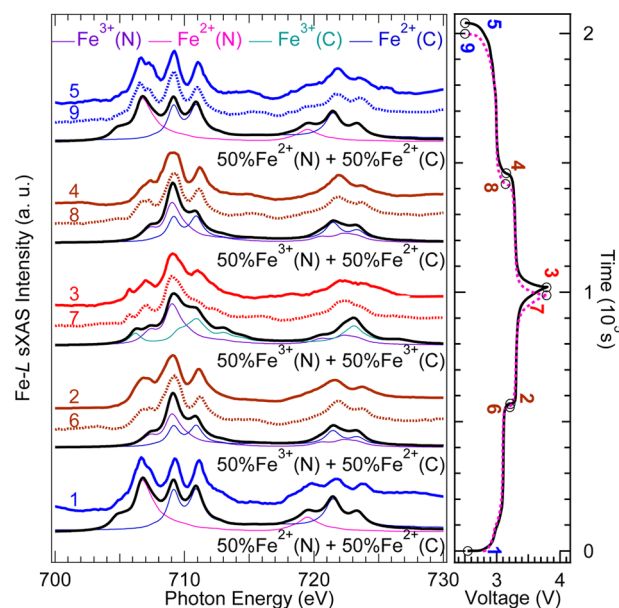

Figure 3. Fe L-edge sXAS spectra (TEY) collected on a series of electrode samples cycled to different electrochemical states. The simulated spectra are shown in black.

sensitivity of the sXAS line shape to a transition-metal valence in a particular ligand field allows a quantitative analysis of the valences of Fe atoms.[14] Because sXAS is also a powerful probe of the ligand-to-metal back bonding, the technique provides an especially site-sensitive probe of the Fe redox centers in Na$_{2-x}$FeHCF.[15,16]

By virtue of the sensitivity to the localized Fe-3d states, Fe-L sXAS of FeC$_6$ and FeN$_6$ octahedra can be accurately modeled by atomic multiplet calculations augmented to include both forward and back bonding.[15] Such an approach allows a direct assignment of the spectroscopic features to the specific site and spin state of Fe atoms. Figure 2 compares theoretical
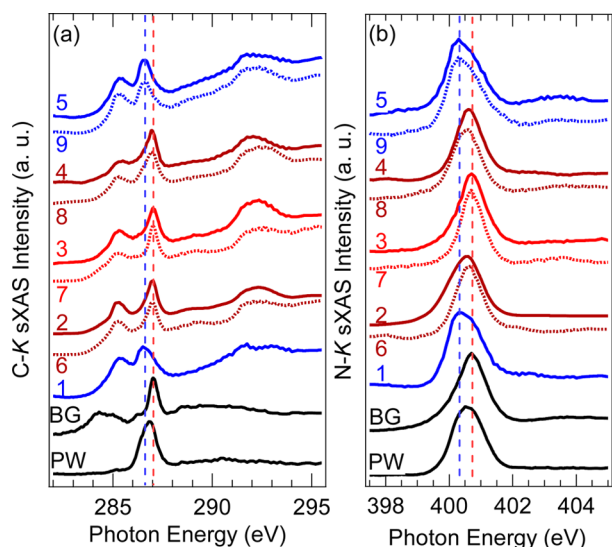
Figure 4. C and N K-edge sXAS spectra (TEY) collected on PW/BG and a series of electrode samples cycled to different electrochemical states.

calculations to the Fe L-edge sXAS of our PW (R-FeHCF) and BG $Fe_2(CN)_6$ samples. Overall, the Fe L-edge sXAS spectra consist of two well-separated L_3 (697−709 eV) and L_2 (713−722 eV) absorption features resulting from core-hole spin−orbit coupling.[17] The calculations in this paper follow those developed by Hocking et al.[15] Our hopping parameters and back-bonding configuration energies have been adjusted to

reproduce the energy splittings observed in the sXAS experiments (see Supporting Information). The back bonding to the empty σ-bonding e states of the LS-Fe^{II}:t^6e^0 configuration of the $Fe^{II}C_6$ octahedra (Fe^{2+}(C)) is particularly strong as shown for the Fe-L_3 sXAS of the $Fe^{II}C_6$ octahedra in Figure 2. The $Fe^{III}C_6$ octahedra (Fe^{3+}(C)) display a low-energy peak at 705.5 eV associated with back-bonding to the π-bonding hole in the t^5 configuration of the LS Fe^{III}: t^5e^0 ion. The low energy 705.5 eV state originates from the transitions to the t_{2g} holes in the d manifold on going from low-spin $Fe^{II}C_6$ to low-spin $Fe^{III}C_6$.[15] For N-coordinated Fe sites, the ligand field is much weaker, resulting in simpler local physics and sXAS spectra that are characteristic of high spin Fe^{3+}(N) and Fe^{2+}(N). As indicated by the dashed vertical lines in Figure 2, the agreement between calculated and experimental sXAS lines is excellent.

Figure 3 shows the Fe L-edge sXAS TEY (TFY spectra in Figure S4) spectra collected on a series of electrode samples cycling twice to different states of charge. The spectra evolve reversibly with cycling in accordance with redox reactions on the Fe centers. As expected, the absorption profiles of the pristine (1) and fully discharged (5 and 9) electrodes are similar to that of the PW; those of the fully charged electrodes (3 and 7) display dramatically different spectra similar to that of BG. Moreover, the half-charged (2 and 6) and half discharged (4 and 8) electrodes of Figure 3 show no sXAS feature at low energies near 705 eV, indicating the missing components of $Fe^{III}C$ and $Fe^{II}N$ that both show peaks at low energies (Figure 2). Indeed, the sum of $Fe^{II}C$ and $Fe^{III}N$ spectra agree well with our experimental spectra of these electrodes with intermediate electrochemical states (Figure 3). This result provides a direct
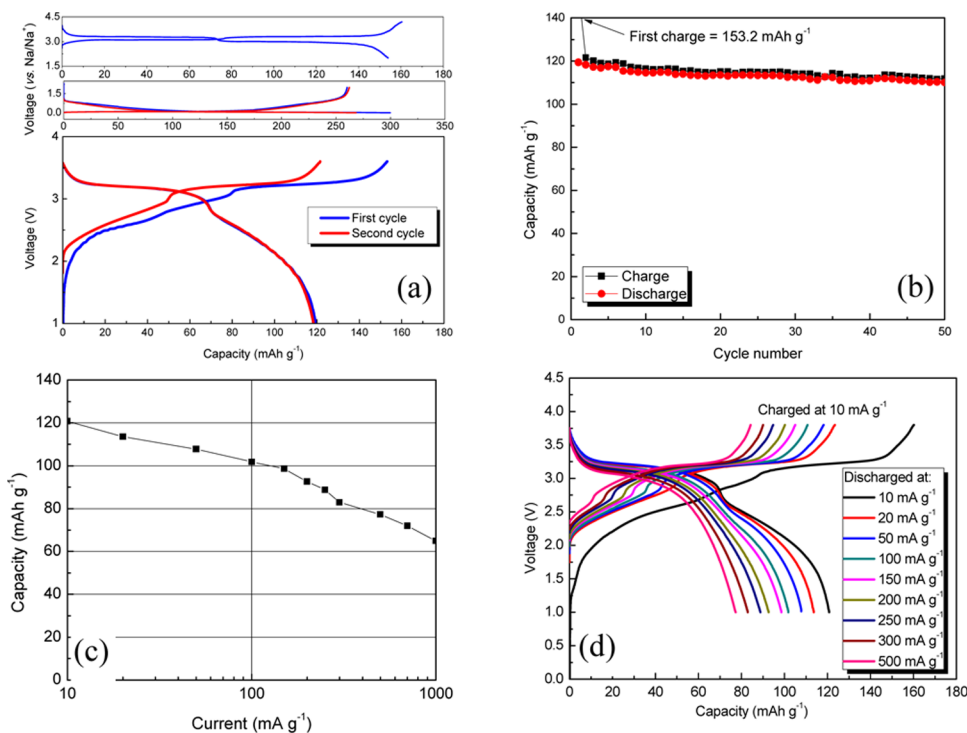

Figure 5. Electrochemical performance of R-FeHCF full cells with hard carbon anode. The cathode consists of 86 wt % R-FeHCF, 7 wt % Kejen black, and 7 wt % PTFE. The anode is made of 95% hard carbon and 5 wt % CMC/SBR. The capacity ratio of anode to cathode is 1.05. The capacity and current are normalized by the mass of active material in the cathode. (a) Galvanostatic charge and discharge curves of R-FeHCF/Na, hard carbon/Na half cells and R-FeHCF/hard carbon full cell at a current of 10 mA g^{-1} at the first cycle. (b) Capacity retention of a R-FeHCF/hard carbon full cell in 50 cycles. It was charged/discharged at the current of 10 mA g^{-1}. (c) Rate capability of the R-FeHCF/hard carbon full cell. It was charged at 10 mA g^{-1} and discharged at different currents. (d) Discharge curves of the R-FeHCF/hard carbon full cell at different currents.

verification that the low-voltage plateau corresponds to a redox reaction on the FeN_6 octahedra, and the high-voltage plateau to a redox reaction on the FeC_6 centers.

The difference between the redox energies of the FeC_6 and FeN_6 centers reflects different Fe-$3d$ energy diagrams that could be fundamentally understood through our sXAS and theory. In a charged electrode, there are 5 Fe^{III}-$3d$ electrons. For the HS-$Fe^{III}N$, all five electrons are of majority spin with t^3e^2 configuration. Adding a minority-spin electron to such a HS system gains no interatomic exchange stabilization and experiences the higher cost of on-site electron−electron coulomb energy. This situation leads to high energies of the unoccupied states (sXAS onset) in HS d^5 system,[18] which prevent the electrons getting onto $Fe^{III}N$ easily. On the contrary, for the LS-$Fe^{III}C$, there is only one unoccupied state in the t^5 configuration. Adding one electron will fill up the t_{2g} band and is thus favored in energy, as shown by the low energy sXAS peak at 705.5 eV in the $Fe^{3+}(C)$ spectrum (Figure 2). Therefore, compared with that of the HS-$Fe^{III}N$, electron-filling (discharging) to the LS-$Fe^{III}C$ is much more energetically favored, leading to the redox of FeC_6 corresponding to the first discharge (high voltage) plateau.

Surprisingly, while the Fe-L sXAS data clearly show that the high and low voltage plateaus correspond to the Fe redox on the C and N sites, respectively, the C and N K-edge sXAS display similar spectral evolutions during electrochemical cycling (Figure 4). The bulk-sensitive TFY sXAS (Figure S5) shows the same behavior as the surface-sensitive TEY results. The energy shifts of the main peaks in the C- and N-K spectra indicate the chemical potential change during the electrochemical operation; i.e., high oxidation states in the charged electrodes (3 and 7) lead to higher energy values of the main peak, compared with the discharged electrodes (1, 5, and 9). In a localized picture, because the high and low voltage plateaus correspond to FeC_6 and FeN_6 redox centers, one would expect the C-K spectra of the electrodes with intermediated electrochemical states (2, 6, 4, and 8) are close to that of the discharged states, and vice versa for N-K. The observation that sXAS of both C- and N-K main peaks evolve in the same way indicates that the electron states in the samples are highly itinerant. Thus, the C and N sXAS data reflect a uniform chemical potential change. The highly itinerant electrons likely contribute to the improved electronic conductivity and the excellent rate performance as shown in Figure 1c,d.

Full Cells. Thanks to the rich sodium-ion content in R-FeHCF, a 3-V full cell was directly assembled with an R-FeHCF cathode and an anode consisting of 95 wt % Kureha hard carbon and 5 wt % CMC/SBR (1:1) binder. A Na half-cell with this anode showed a first-cycle Coulombic efficiency of 86%; the irreversible capacity of the first cycle comes mainly from formation of an SEI layer on the hard carbon electrode. Regarding to excess hard carbon, the gravimetric numbers presented here are normalized by the mass of R-FeHCF. At 10 mA g^{-1}, the full cell showed an initial charge capacity of 153.1 mAh g^{-1} and a discharge capacity of 119.4 mAh g^{-1}, corresponding to an initial Coulombic efficiency of 78%, Figure 5a. The lower Coulombic efficiency of the full cell was ascribed to the 5% excess hard carbon in the full-cell assembly. A good cycling performance was obtained after the first cycle with 94% capacity retention after 50 cycles, Figure 5b.

The poor diffusion of Na in hard carbon[19] compromised the rate performance of the full cell compared to that of the half-cell. Nevertheless, 67% of the initial capacity was retained at

500 mAh g^{-1} (3.3C), Figure 5c,d. A better rate capability can be expected from a Na-ion battery with R-FeHCF cathode when a superior anode material becomes available.

To check the ability to manufacture such a discharged full sodium-ion battery at low cost within dry-air rooms of existing lithium-ion battery infrastructures, the stability of the R-FeHCF was examined after the electrode was placed in dry air for 20 h. Figure S7 shows there was no significant difference in battery performance after a 20-h dry-air exposure compared to that with an as-synthesized R-FeHCF electrode. A thin PB surface phase on the PW electrode, deduced from the Raman spectrum, is believed to inhibit further oxidation of the PW on exposure to dry air.

■ CONCLUSIONS

A dehydrated air-stable R-FeHCF with few $Fe(CN)_6$ vacancies is a promising electrode material for a Na-ion battery. The key advantage of this material is the high Na concentration. It can be assembled in a discharged state in a full cell with an anode containing no sodium. Such a full cell has demonstrated a high capacity, good rate performance, and long cycle life. The electrochemical cycling of such materials is strongly regulated by the Fe-3d states with different spin states at different sites. Scientifically, our soft X-ray spectroscopic results clarify the mechanism of the electrochemical performance. Technically, our work enables the possibilities to realize scalable Na-ion battery manufacture utilizing current Li-ion battery infrastructure.

■ EXPERIMENTAL SECTION

Material Synthesis. Three millimoles (mmol) of $Na_4Fe(CN)_6$ were dissolved in 100 mL of distilled water. Ascorbic acid was used to adjust the solution pH to 6.5. The solution was transferred into a Teflon autoclave that was maintained at 140 °C for 20 h with vigorous stirring. The product was washed two times by distilled water and one time with acetone before drying at 120 °C under a vacuum overnight.

Material Characterization. The thermogravimetric analyses were collected on a Perkin−Elmer TGA 7 system in flowing N_2. X-ray diffraction (XRD) patterns were collected on a Rigaku R-Axis Spider diffractometer with an image plate detector, a graphite monochromator and Cu Kα radiation (l = 1.5418 Å). All the XRD samples were sealed in 0.3 mm glass capillaries in an Ar-filled glovebox. Elemental analysis was carried out with energy-dispersive X-ray spectroscopy. Diffraction scanning transmission electron microscopy (D-STEM) was carried out with a JEOL 2010F TEM system.

Electrochemical Evaluation. Electrochemical performances were evaluated with standard CR2032 coin cells. The R-FeHCF electrode consisted of 86 wt % active material, 7 wt % Ketjen black and 7 wt % polytetrafluoroethylene (PTFE) binder. The typical electrode mass was 3−5 mg. In general, the electrolyte comprised 1 mol L^{-1} NaPF$_6$ in a mixture of ethylene carbonate (EC) and diethyl carbonate (DEC) [EC/DEC = 1:1 in volume]. When cycling performance of cells were investigated, 5 wt % fluoroethylene carbonate (FEC) was added into the electrolyte. In half-cells, a Whatman glass-fiber separator was used to insulate the FeHCF electrode and sodium metal counter electrode. In the preparation of full cells, a hard carbon anode with 95 wt % Kureha hard carbon and 5 wt % sodium carboxymethyl cellulose/styrene−butadiene rubber (CMC/SBR) binder was used. One layer of Celgard film was used to separate the cathode and hard carbon anode. All coin cells were assembled in an argon-filled glovebox. The cells were aged for 5 h before charge/discharge to ensure full absorption of electrolyte into the electrodes.

Soft X-ray Spectroscopy (sXAS). sXAS was performed at Beamline 8.0.1 of the Advanced Light Source (ALS) at Lawrence Berkeley National Laboratory (LBNL). The undulator and spherical grating monochromator supply a linearly polarized photon beam with

resolving power up to 6000.[20] The experimental energy resolution is 0.1−0.15 eV. Data were collected in both total-electron-yield (TEY) and total-fluorescence-yield (TFY) modes simultaneously, corresponding to a probe depth of about 10 nm (for TEY) and 100 nm (for TFY). All the spectra have been normalized to the beam flux measured by the upstream gold mesh. sXAS measurements of Fe *L*-edge, C and N *K*-edge were conducted on a series of electrodes that were electrochemically cycled to the desired state of charge. All electrodes were vigorously rinsed with DMC and dried in an Ar glovebox immediately after cell disassembly to lock in the state of charge. Electrodes were transferred into an ultrahigh vacuum sXAS end station through our special sample transfer kit to avoid any air exposure.

sXAS Calculations. Atomic multiplet calculations of Fe *L*-edge sXAS are based closely on the model and notation in ref 15. The configuration energies of different Fe valence states without a core hole is set by parameters $E_{G2} = E_0 - E_L^-$ and $E_{G3} = E_L^- - E_L^+$. The terms E_0, E_L^- and E_L^+ are, respectively, the configuration averaged energies with nominal Fe electron number, with a single hole transferred from Fe to the surrounding cyano groups, or with a single electron transferred from the surrounding cyano groups. Identically defined parameters E_{F2} and E_{F3} apply to the core hole states.

The configuration energies used to describe Fe^{III} at the carbon site are 10 Dq = 4.0 eV, E_{G2} = 0.2 eV, E_{F2} = −0.3 eV, E_{G3} = 1.80 eV, E_{F3} = 2.30 eV. Mixing parameters are 0.9 eV for σ back-bonding, 2.0 eV for π back-bonding, 2.1 eV for σ bonding and 0.6 eV for π bonding. These parameters are identical to the optimized parameter set for $K_3Fe(CN)_6$ in ref 15, with the exception that E_L^- has been raised by 0.8 eV in the ground and intermediate states.

The configuration energies used to describe Fe^{II} at the carbon site are 10 Dq = 3.9 eV, E_{G2} = 3.26 eV, E_{F2} = 2.76 eV, E_{G3} = −3.20 eV, E_{F3} = −1.2 eV. Mixing parameters are 1.2 eV for σ back-bonding, 1.92 eV for π back-bonding, 2.28 eV for σ bonding and 0.0 eV for π bonding. These parameters are identical to the optimized parameter set for $K_4Fe(CN)_6$ in ref 15, with the exception that E_L^- has been lowered by 1.2 eV in the ground and intermediate states and all mixing parameters have been increased by 20%.

N site calculations use reduced 10 Dq values to achieve a high spin state and are performed without a back-bonding mixing parameter. The configuration energies used to describe Fe^{III} at the N site are 10 Dq = 1.0 eV, E_{G2} = 1.0 eV, E_{F2} = 0.5 eV, E_{G3} = −1.5 eV, E_{F3} = 1.0 eV. Mixing parameters are 0 eV for back-bonding, 2.1 eV for σ bonding and 0.6 eV for π bonding. The configuration energies used to describe Fe^{II} at the N site are 10 Dq = 0.7 eV, E_{G2} = 2.06 eV, E_{F2} = −4 eV, E_{G3} = −2 eV, E_{F3} = 1.0 eV. Mixing parameters are 0 eV for back-bonding, 1.9 eV for σ bonding and 0 eV for π bonding.

■ ASSOCIATED CONTENT

Ⓢ Supporting Information

Figure S1: Structural characterization of R-FeHCF. (a) X-ray powder diffraction (XRD) pattern (λCu) of R-FeHFC that is indexed as R$\bar{3}$ symmetric space group with the lattice parameters of $a = b = 6.548(1)$ Å, $c = 18.931(3)$ Å. (b) TGA curves, (c) D-STEM electron diffraction pattern from a particle showing the rhombohedral structure (R$\bar{3}$) viewed down the [241] zone axis, and (d) morphology of R-FeHFC. Figure S2: Structural characterization of R-FeHCF electrode during the first cycle. (a) Ex situ XRD patterns. Asterisks indicated the formation of an intermediate phase when a phase transition took place between the rhombohedral and cubic structure; and (b) stretching vibration of cyano bond in ex situ Raman spectra. Figure S3: Fe *L*-edge SXAS spectra (TFY) collected on PW/BG and a series of electrodes cycled to different electrochemical states. Figure S4: C and N *K*-edge sXAS spectra (TFY) collected on PW/BG and a series of electrodes cycled to different electrochemical states. Figure S5: Na *K*-edge SXAS spectra (TEY and TFY) collected on a series of electrodes cycled to different electrochemical states. Figure

S6: Electrochemical performance of R-FeHCF electrode exposed to air for 20 h. The charge/discharge current is 1 C (150 mA g^{-1}). (a) Its capacity retention and (b) its galvanostatic charge and discharge curves at the first cycle. This material is available free of charge via the Internet at http://pubs.acs.org.

■ AUTHOR INFORMATION

Corresponding Author
luy@sharplabs.com

Author Contributions
$^\nabla$L.W. and J.S. contributed equally.

Notes
The authors declare no competing financial interest.

■ REFERENCES

(1) Yabuuchi, N.; Kajiyama, M.; Iwatate, J.; Nishikawa, H.; Hitomi, S.; Okuyama, R.; Usui, R.; Yamada, Y.; Komaba, S. *Nat. Mater.* **2012**, *11*, 512.

(2) Palomares, V.; Casas-Cabanas, M.; Castillo-Martínez, E.; Han, M. H.; Rojo, T. *Energy Environ. Sci.* **2013**, *6*, 2312.

(3) Wessells, C. D.; McDowell, M. T.; Peddada, S. V.; Pasta, M.; Huggins, R. A.; Cui, Y. *ACS Nano* **2012**, *6*, 1688.

(4) Wessells, C. D.; Huggins, R. A.; Cui, Y. *Nat. Commun.* **2011**, *2*, 550.

(5) Lu, Y.; Wang, L.; Cheng, J. G.; Goodenough, J. B. *Chem. Commun.* **2012**, *48*, 6544.

(6) Wang, L.; Lu, Y.; Liu, J.; Xu, M.; Cheng, J.; Zhang, D.; Goodenough, J. B. *Angew. Chem., Int. Ed.* **2013**, *52*, 1964.

(7) Wu, X.; Deng, W.; Qian, J.; Cao, Y.; Ai, X.; Yang, H. *J. Mater. Chem. A* **2013**, *1*, 10130.

(8) You, Y.; Yu, X.-Q.; Yin, Y.-X.; Nam, K.-W.; Guo, Y.-G. *Nano Res.* **2015**, *8*, 117.

(9) Kareis, C. M.; Lapidus, S. H.; Her, J. H.; Stephens, P. W.; Miller, J. S. *J. Am. Chem. Soc.* **2012**, *134*, 2246.

(10) Pajerowski, D. M.; Watanabe, T.; Yamamoto, T.; Einaga, Y. *Phys. Rev. B: Condens. Matter Mater. Phys.* **2011**, *83*, 153202.

(11) Yang, W.; Liu, X.; Qiao, R.; Olalde-Velasco, P.; Spear, J. D.; Roseguo, L.; Pepper, J. X.; Chuang, Y.-D.; Denlinger, J. D.; Hussain, Z. *J. Electron Spectrosc. Relat. Phenom.* **2013**, *190*, 64.

(12) Qiao, R.; Lucas, I. T.; Karim, A.; Syzdek, J.; Liu, X.; Chen, W.; Persson, K.; Kostecki, R.; Yang, W. *Adv. Mater. Inter.* **2014**, *1*, 1300115.

(13) Liu, X.; Wang, D.; Liu, G.; Srinivasan, V.; Liu, Z.; Hussain, Z.; Yang, W. *Nat. Commun.* **2013**, *4*, 2568.

(14) Liu, X.; Liu, J.; Qiao, R.; Yu, Y.; Li, H.; Suo, L.; Chuang, Y.-D.; Shu, G.; Chou, F.; Weng, T.-C.; Nordlund, D.; Sokaras, D.; Wang, Y. J.; Lin, H.; Barbiellini, B.; Bansil, A.; Song, X.; Liu, Z.; Yan, S.; Liu, G.; Qiao, S.; Richardson, T. J.; Prendergast, D.; Hussain, Z.; de Groot, F. M. F.; Yang, W. *J. Am. Chem. Soc.* **2012**, *134*, 13708.

(15) Bonhommeau, S.; Pontius, N.; Cobo, S.; Salmon, L.; de Groot, F. M. F.; Molnár, G.; Bousseksou, A.; Dürr, H. A.; Eberhardt, W. *Phys. Chem. Chem. Phys.* **2008**, *10*, 5882.

(16) Hocking, R. K.; Wasinger, E. C.; de Groot, F. M. F.; Hodgson, K. O.; Hedman, B.; Solomon, E. I. *J. Am. Chem. Soc.* **2006**, *128*, 10442.

(17) de Groot, F.; Kotani, A.; *Core Level Spectroscopy of Solids*; CRC Press Taylor & Francis Group: Boca Raton, FL, 2008.

(18) Olalde-Velasco, P.; Jimenez-Mier, J.; Denlinger, J. D.; Hussain, Z.; Yang, W. L. *Phys. Rev. B: Condens. Matter Mater. Phys.* **2011**, *83*, 241102.

(19) Ponrouch, A.; Goñi, A. R.; Palacín, R. M. *Electrochem. Commun.* **2013**, *27*, 85.

(20) Jia, J. J.; Callcott, T. A.; Yurkas, J.; Ellis, A. W.; Himpsel, F. J.; Samant, M. G.; Stöhr, J.; Ederer, D. L.; Carlisle, J. A.; Hudson, E. A.; Terminello, L. J.; Shuh, D. K.; Perera, R. C. C. *Rev. Sci. Instrum.* **1995**, *66*, 1394.